

STATIC STABILITY STUDY OF STIFFENED FUNCTIONALLY GRADED COMPOSITE PLATES REINFORCED BY CARBON NANOTUBES USING FINITE ELEMENT METHOD

Nguyen Thai Chung^{1,*}, Duong Thi Ngoc Thu²

¹*Department of Solid Mechanics, Le Quy Don Technical University, Hanoi, Vietnam*

²*University of Transport Technology, Hanoi, Vietnam*

*E-mail: chungnt@mta.edu.vn

Received: 09 September 2023 / Published online: 30 September 2023

Abstract. This paper presents some results on the linear stability research of Stiffened Functionally Graded Carbon NanoTube-Reinforced Composite (SFG-CNTRC) plates under static in-plane loads by the Finite Element Method (FEM) and a new four-variable refined plate theory. The governing equations for the static buckling of the system are obtained by the new four-variable refined plate theory and FEM. The eigenvalue problem method was used to solve the equation to determine the critical force of the plates. A numerical example is compared with the results in another research to check the validity of the present algorithm. The influences of some factors such as plate theory, CNT distribution along the layer thickness, stiffener height ratio, and fiber orientation angle on the critical buckling loads and unstable regions are discussed.

Keywords: stability, nanotubes reinforced, unstable regions, stiffened.

1. INTRODUCTION

With the development of advanced materials science and the optimization of structures, some new types of structures such as beams, plates, and shells are made of functionally graded composite materials with reinforced by nanotubes carbon have been applied in the automotive, nuclear, aerospace, and mechatronic industries. In fact, the damage of the above structures due to instability under the type loads is quite common and is being studied by scientists.

Lei et al. [1] used the element-free kp-Ritz method to establish the buckling equation of the Functionally Graded Carbon NanoTube-Reinforced Composite (FG-CNTRC)

plates subjected to in-plane compress loads. In this study, the first-order shear deformation plate theory is used. By FEM too, Chung et al. [2] studied the dynamic buckling of piezoelectric composite plates subjected to in-plane loads. In this research, the damping forces of the system have been considered. Also, the effects of loads, piezoelectric properties, and plate thickness on buckling of the plate are investigated by numerical examples. Zhang et al. [3] studied the buckling properties of FG-CNTRC plates subjected to static loads using the element-free IMLS-Ritz method. Shahidi et al. [4] analyzed effect of some factors on critical buckling loads of triangular nano-composite plates on Winkler-Pasternak elastic foundation subjected to uniform in-plane static compression loads using the classical plate theory and FEM. Moradi-Dastjerdi and Malek-Mohammad [5], Civalek, and Avcar [6] have applied the refined plate theory to research on free vibration and static instability of functionally graded nanocomposite plates reinforced by aggregated carbon nanotube. In this study, the effect of CNT volume fraction, Carbon NanoTube (CNT) distribution, CNT cluster distribution, and geometric dimensions of the plate on the natural frequency and critical buckling loads are considered. Bash et al. [7] used FEM to study linear and nonlinear buckling of composite plates with rectangular cutouts, in there the effect of size of rectangular cutouts on the buckling critical loads are investigated. Thanh [8] used the Airy's stress function and Galerkin method to study nonlinear stability and post-buckling of stiffened nanocomposite functionally graded plates reinforced by carbon nanotubes on elastic foundations subjected to mechanical and thermal loads. Minh et al. [9] studied the nonlinear stability of FG-CNTRC plates under axial compression load using higher-order shear deformation plate theory. Liu et al. [10] analyzed the effect of plate theory (classical plate theory and refined plate theory) on static, free vibration, stability, and dynamic response of FG-CNTRC) plates. Meiche et al. [11] have determined the critical buckling loads and vibration characteristics of the FGM sandwich plates using a new refined hyperbolic shear deformable plate theory with only four unknown functions. Thai and Vo [12], Thai and Kim [13] used new function shear deformation theory too, but by sin function on bending, stability, and vibration analysis of FG plates. In their study, Daouadji et al. [14] used a new higher-order shear deformation theory on static analysis of FG plates. Chung et al [15] analyzed the dynamic of the stiffened functionally graded composite plates reinforced by carbon nanotubes (SFG-CNTRC) under a blast load system using FEM and a new polynomial shear deformation function.

This paper presented the static buckling analysis of SFG-CNTRC plates subjected to in-plane loads based on new shear strain functions and in different boundary conditions. In this study, the four-variable refined plate theory developed by us has been extended for the first time to the static buckling behavior of SFG-CNTRC plate. The influence of the CNT distribution along the layer thickness, CNTs' volume fractions, as well as loads, geometrical parameters, and stiffeners on the critical buckling load and unstable regions

of SFG-CNTRC plates are investigated. The new contents of this paper are the effect of stiffener stiffness on the algorithm based on the new shear strain function and the finite element method. The unstable regions of SFG-CNTRC plates are also excellent results of the article.

2. MATERIAL PROPERTIES OF SFG-CNTRC

In this study, a functionally graded carbon nanotube-reinforced laminated stiffened composite rectangular plate was subjected to in-plane static compression forces. The geometric model of the problem is shown in Fig. 1. In Fig. 1, four typical FG-CNTRC rectangular plates (UD, FG-V, FG-O, and FG-X) with length a , width b , and total thickness h are considered in this study.

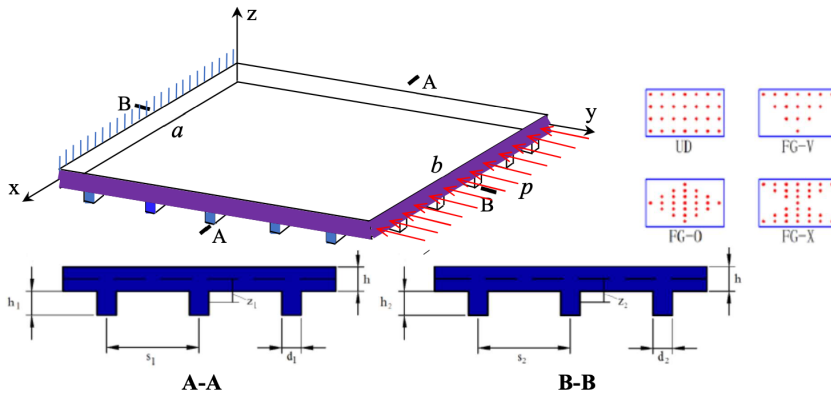


Fig. 1. The structure of a SFG-CNTRC and load subjected to the plate

In all distributions, the law of uniform distribution (UD) is the uniform distribution of CNTs in the cross-section of the plate, while the law of asymmetrical distribution (FG-V) or symmetrical distributions (FG-O, FG-X) is the dependence of the density of CNTs on the plate thickness variable. Accordingly, the mathematical model of the distribution of CNTs along the thickness direction of the plate is as follows [15–19]:

$$\begin{cases} V_{CNT} = V_{CNT}^* & \text{(UD),} \\ V_{CNT}(z) = (1 + 2z/h) V_{CNT}^* & \text{(FG-V),} \\ V_{CNT}(z) = 2(1 - 2|z|/h) V_{CNT}^* & \text{(FG-O),} \\ V_{CNT}(z) = 4|z|/h V_{CNT}^* & \text{(FG-X),} \end{cases} \quad (-h/2 \leq z \leq h/2) \quad (1)$$

where V_{CNT}^* is the volume fraction of the CNTs defined by:

$$V_{CNT}^* = w_{CNT} / (w_{CNT} + (\rho_{CNT} / \rho_m) (1 - w_{CNT})), \quad (2)$$

with w_{CNT} is the mass fraction of the CNTs, and ρ_{CNT} and ρ_m are the densities of the CNTs and the matrix, respectively. The effective properties of the FG-CNTRC lamina can be determined as follows [10, 15, 19]:

$$\begin{cases} E_{11} = \eta_1 V_{CNT} E_{11}^{CNT} + V_m E^m, \\ \eta_2/E_{22} = V_{CNT}/E_{22}^{CNT} + V_m/E^m, \\ \eta_3/G_{12} = V_{CNT}/G_{12}^{CNT} + V_m/G^m, \end{cases} \quad (3)$$

where $E_{11}^{CNT}, E_{22}^{CNT}$ are Young's moduli of the CNTs; G_{12}^{CNT} is the shear modulus of the CNT, E^m , and G^m are Young's modulus and shear modulus of the polymer matrix, respectively; η_1, η_2 and η_3 denote the CNT efficiency parameters; V_{CNT}, V_m are the volume fractions of the CNT and the polymer matrix, which are defined as:

$$V_{CNT} + V_m = 1. \quad (4)$$

The material properties of the FG-CNTRC plates are determined as:

$$\begin{cases} \rho = V_{CNT} \rho_{CNT} + V_m \rho_m, \\ \nu_{12} = V_{CNT}^* \nu_{12}^{CNT} + V_m \nu^m, \end{cases} \quad (5)$$

where ν^m is the Poisson's ratio of the matrix.

In the case where ν_{12} is constant along the thickness of the FG-CNTRC plate and the material is isotropic, we have:

$$\begin{cases} E_{33} = E_{22}, & G_{12} = G_{13} = G_{23}, \\ \nu_{13} = \nu_{12}, & \nu_{31} = \nu_{21}, \quad \nu_{32} = \nu_{23} = \nu_{21}, \quad \nu_{21} = E_{22} \nu_{12} / E_{11}. \end{cases} \quad (6)$$

3. FUNDAMENTAL EQUATIONS

3.1. Stability equations of FG-CNTRC plate element under in-plane loading

Using the four-variable refined plate theory, the displacement components as [12, 15, 20–22]:

$$\begin{aligned} u(x, y, z) &= u_0(x, y) - z \partial w_b(x, y) / \partial x - f(z) \partial w_s(x, y) / \partial x, \\ v(x, y, z) &= v_0(x, y) - z \partial w_b(x, y) / \partial y - f(z) \partial w_s(x, y) / \partial y, \\ w(x, y, z) &= w_b(x, y) + w_s(x, y), \end{aligned} \quad (7)$$

in which u_0, v_0 , and w_0 are the displacements of the corresponding point on the mid-plane, respectively; w_b and w_s denote the bending and shear components of the transverse displacement, respectively; $f(z)$ is the correction function of the transverse shear strains. In this study, the correction function of shear strain is determined as follows [15]:

$$f(z) = z \left(1/4 + \frac{z^2}{h^2} \right). \quad (8)$$

The nonlinear von Karman strain-displacement equations are as follows [19]:

$$\{\varepsilon\} = \begin{Bmatrix} \varepsilon_x \\ \varepsilon_y \\ \gamma_{xy} \\ \gamma_{yz} \\ \gamma_{xz} \end{Bmatrix} = \begin{Bmatrix} \varepsilon_x^{0L} + z\kappa_x^b + f(z)\kappa_x^s \\ \varepsilon_y^{0L} + z\kappa_y^b + f(z)\kappa_y^s \\ \gamma_{xy}^{0L} + z\kappa_{xy}^b + f(z)\kappa_{xy}^s \\ h(z)\gamma_{yz}^s \\ h(z)\gamma_{xz}^s \end{Bmatrix} + \begin{Bmatrix} \varepsilon_x^{0NL} \\ \varepsilon_y^{0NL} \\ \gamma_{xy}^{0NL} \\ 0 \\ 0 \end{Bmatrix} = \{\varepsilon\}_1 + \{\varepsilon\}_2, \quad (9)$$

where $\{\varepsilon\}_1$ and $\{\varepsilon\}_2$ represent the linear and nonlinear parts of the strain:

$$\{\varepsilon\}_1 = \begin{Bmatrix} \varepsilon_x^{0L} + z\kappa_x^b + f(z)\kappa_x^s \\ \varepsilon_y^{0L} + z\kappa_y^b + f(z)\kappa_y^s \\ \gamma_{xy}^{0L} + z\kappa_{xy}^b + f(z)\kappa_{xy}^s \\ h(z)\gamma_{yz}^s \\ h(z)\gamma_{xz}^s \end{Bmatrix} = \begin{Bmatrix} \frac{\partial u_0}{\partial x} - z\frac{\partial^2 w_b}{\partial x^2} - f(z)\frac{\partial^2 w_s}{\partial x^2} \\ \frac{\partial v_0}{\partial y} - z\frac{\partial^2 w_b}{\partial y^2} - f(z)\frac{\partial^2 w_s}{\partial y^2} \\ \left(\frac{\partial v_0}{\partial x} + \frac{\partial u_0}{\partial y}\right) - 2z\frac{\partial^2 w_b}{\partial x\partial y} - 2f(z)\frac{\partial^2 w_s}{\partial x\partial y} \\ h(z)\frac{\partial w_s}{\partial y} \\ h(z)\frac{\partial w_s}{\partial x} \end{Bmatrix}, \quad (10)$$

$$\begin{aligned} \{\varepsilon\}_2 &= \frac{1}{2} \begin{Bmatrix} \left(\frac{\partial w_b}{\partial x} + \frac{\partial w_s}{\partial x}\right)^2 \\ \left(\frac{\partial w_b}{\partial y} + \frac{\partial w_s}{\partial y}\right)^2 \\ 2\left(\frac{\partial w_b}{\partial x} + \frac{\partial w_s}{\partial x}\right)\left(\frac{\partial w_b}{\partial y} + \frac{\partial w_s}{\partial y}\right) \\ 0 \\ 0 \end{Bmatrix} \\ &= \frac{1}{2} \begin{bmatrix} \frac{\partial(w_b + w_s)}{\partial x} & 0 \\ 0 & \frac{\partial(w_b + w_s)}{\partial y} \\ \frac{\partial(w_b + w_s)}{\partial y} & \frac{\partial(w_b + w_s)}{\partial x} \end{bmatrix} \begin{Bmatrix} \frac{\partial(w_b + w_s)}{\partial x} \\ \frac{\partial(w_b + w_s)}{\partial y} \end{Bmatrix}. \end{aligned} \quad (11)$$

The constitutive relations for each FG-CNTRC layer can be expressed as follows [19,23]:

$$\begin{Bmatrix} \sigma_x \\ \sigma_y \\ \tau_{xy} \\ \tau_{xz} \\ \tau_{yz} \end{Bmatrix}^k = \begin{bmatrix} \bar{Q}_{11} & \bar{Q}_{12} & \bar{Q}_{16} & 0 & 0 \\ \bar{Q}_{12} & \bar{Q}_{22} & \bar{Q}_{26} & 0 & 0 \\ \bar{Q}_{16} & \bar{Q}_{26} & \bar{Q}_{66} & 0 & 0 \\ 0 & 0 & 0 & \bar{Q}_{44} & \bar{Q}_{45} \\ 0 & 0 & 0 & \bar{Q}_{45} & \bar{Q}_{55} \end{bmatrix}^k \begin{Bmatrix} \varepsilon_x \\ \varepsilon_y \\ \gamma_{xy} \\ \gamma_{xz} \\ \gamma_{yz} \end{Bmatrix}, \quad (12)$$

where \bar{Q}_{ij}^k are the transformed elastic coefficients, they are determined as shown in [15].

For each FG-CNT layer, we have:

$$\begin{aligned} Q_{11}^k &= E_{11}(z)/(1 - \nu_{12}\nu_{21}), & Q_{12}^k &= Q_{21}^k = \nu_{12}E_{22}(z)/(1 - \nu_{12}\nu_{21}), \\ Q_{22}^k &= E_{22}(z)/(1 - \nu_{12}\nu_{21}), & Q_{44}^k &= G_{23}^k, & Q_{55}^k &= G_{13}^k, & Q_{66}^k &= G_{12}^k. \end{aligned} \quad (13)$$

The stability equation of the plate element can be obtained by minimizing the total potential energy as follows [21, 23]:

$$\delta U + \delta W = 0, \quad (14)$$

where $\delta U, \delta W$ are the virtual linear strains energy and the virtual work of the plate element, respectively.

By FEM, in-plane and transverse displacements determined as follow:

$$\begin{aligned} u_0(x, y, t) &= \sum_{j=1}^4 \Delta u_j^0 \Psi_j(x, y) = \mathbf{n}^T \Delta \mathbf{u}_0, & v_0(x, y, t) &= \sum_{j=1}^4 \Delta v_j^0 \Psi_j(x, y) = \mathbf{n}^T \Delta \mathbf{v}_0, \\ w_b(x, y, t) &= \sum_{j=1}^4 \Delta w_j^b \Phi_j(x, y) = \mathbf{N}^T \Delta \mathbf{w}_b, & w_s(x, y, t) &= \sum_{j=1}^4 \Delta w_j^s \Phi_j(x, y) = \mathbf{N}^T \Delta \mathbf{w}_s, \end{aligned} \quad (15)$$

where $\Delta \mathbf{u}_0, \Delta \mathbf{v}_0, \Delta \mathbf{w}_b,$ and $\Delta \mathbf{w}_s$ are the in-plane, transverse DOF vectors, Ψ_j and Φ_j are interpolation functions, \mathbf{n} and \mathbf{N} are shape functions, respectively.

The virtual linear strains energy [22, 23]:

$$\delta U = \int_V \delta \{\varepsilon\}_1^T \{\sigma\}, \quad (16)$$

Substituting (15) into (10), we have:

$$\delta \{\varepsilon\}_1 = [B] \{\delta q_e\}, \quad (17)$$

where $\delta \{q_e\} = \delta \{\Delta \mathbf{u}_0 \quad \Delta \mathbf{v}_0 \quad \Delta \mathbf{w}_b \quad \Delta \mathbf{w}_s\}^T$ and $[B]$ is the derivative matrix, shown in Appendix A.

Substituting (12), (17) into (16) leads to:

$$\delta U = \int_A \delta \{\varepsilon\}_1^T \left(\sum_{k=1}^N \int_{h_k}^{h_{k+1}} [\bar{Q}_k] \right) \{\varepsilon\}_1 dA dz = \int_A ([B] \{\delta q_e\})^T [C] ([B] \{q_e\}) dA, \quad (18)$$

where $[C] = \sum_{k=1}^N \int_{h_k}^{h_{k+1}} [\bar{Q}_k] dz$. Hence, the virtual strain energy [21, 23]:

$$\delta U = \{\delta q_e\}^T \int_A [B]^T [C] [B] \{q_e\} dA = \{\delta q_e\}^T [K_e] \{q_e\}, \quad (19)$$

where $[K_e]$ is the element stiffness matrix:

$$[K_e] = \int_A [B]^T [C] [B] dA. \quad (20)$$

Now, by Eqs. (11) and (15) we have:

$$\delta \{\varepsilon\}_2 = \frac{1}{2} \begin{bmatrix} \frac{\partial N^T}{\partial x} \delta (\Delta w_b + \Delta w_s) & 0 \\ 0 & \frac{\partial N^T}{\partial y} \delta (\Delta w_b + \Delta w_s) \\ \frac{\partial N^T}{\partial y} \delta (\Delta w_b + \Delta w_s) & \frac{\partial N^T}{\partial x} \delta (\Delta w_b + \Delta w_s) \end{bmatrix} \left\{ \begin{array}{l} \frac{\partial N^T (\Delta w_b + \Delta w_s)}{\partial x} \\ \frac{\partial N^T (\Delta w_b + \Delta w_s)}{\partial y} \end{array} \right\}. \quad (21)$$

The virtual work:

$$\delta W = \delta \{q_e\}^T \int_A [D]^T [R] [D] \{q_e\} dA, \quad (22)$$

where

$$[D] = \begin{bmatrix} 0 & 0 & 0 & 0 \\ 0 & 0 & 0 & 0 \\ 0 & 0 & \frac{\partial N^T}{\partial x} & \frac{\partial N^T}{\partial x} \\ 0 & 0 & \frac{\partial N^T}{\partial y} & \frac{\partial N^T}{\partial y} \end{bmatrix}, [R] = \begin{bmatrix} 0 & 0 & 0 & 0 \\ 0 & 0 & 0 & 0 \\ 0 & 0 & R_x & R_{xy} \\ 0 & 0 & R_{xy} & R_y \end{bmatrix}, \left\{ \begin{array}{l} R_x \\ R_y \\ R_{xy} \end{array} \right\} = \sum_{k=1}^N \int_{h_k}^{h_{k+1}} \left\{ \begin{array}{l} \sigma_x \\ \sigma_y \\ \tau_{xy} \end{array} \right\}^k dz.$$

Now, let $R_x = p_0$, $R_y = \eta p_0$, $R_{xy} = \xi p_0$, leads to:

$$\delta W = \delta \{q_e\}^T p_0 [K_{eG}] \{q_e\}, \quad (23)$$

where

$$[K_{eG}] = \int_A [D]^T \begin{bmatrix} 1 & \xi \\ \xi & \eta \end{bmatrix} [D] dA, \quad (24)$$

with $[K_{eG}]$ is the element geometric stiffness matrix.

Substituting (19), (23) leads to:

$$\{\delta q_e\}^T [K_e] \{q_e\} + \delta \{q_e\}^T p_0 [K_{eG}] \{q_e\} = 0. \tag{25}$$

Sine $\{\delta q_e\}^T$ is arbitrary and cannot be equal to zero, it follows that:

$$([K_e] + p_0 [K_{eG}]) \{q_e\} = 0, \tag{26}$$

where $\{q_e\} = \{\Delta u_0 \ \Delta v_0 \ \Delta w_b \ \Delta w_s\}^T$ is the element nodal displacement vector of the 4-node rectangular element as follows:

$$\begin{aligned} \Delta u_0 &= \{ u_0^1 \ u_0^2 \ u_0^3 \ u_0^4 \}^T, \Delta v_0 = \{ v_0^1 \ v_0^2 \ v_0^3 \ v_0^4 \}^T, \\ \Delta w_b &= \left\{ w_b^1 \ (\partial w_b / \partial y)^1 \ (-\partial w_b / \partial x)^1 \ \dots \ (-\partial w_b / \partial x)^4 \right\}^T, \\ \Delta w_s &= \left\{ w_s^1 \ (\partial w_s / \partial y)^1 \ (-\partial w_s / \partial x)^1 \ \dots \ (-\partial w_s / \partial x)^4 \right\}^T. \end{aligned} \tag{27}$$

3.2. Functionally graded composite stiffener subjected to compressive axial loads

The displacement field is given as [23–26]]:

$$\begin{cases} U(x, z) = u_0(x) - zdw_0(x)/dx, \\ W(x, z) = w_0(x), \end{cases} \tag{28}$$

where u_0 - axial displacement, w_0 - bending components of the transverse displacement.

The linear strain-displacement relation can be determined as:

$$\epsilon_{xx} = \frac{dU}{dx} = \frac{du_0}{dx} - z \frac{d^2w_0}{dx^2}. \tag{29}$$

For each orthotropic lamina, the linear stress-strain relation is given by:

$$\sigma_{xx}^k = Q_{11}^k \epsilon_{xx}, \tag{30}$$

where $Q_{11}^k = E_f(z) / (1 - \nu_f^2)$, $E_f(z) = (E_m - E_c)(z/h_i + 1/2) + E_c$ and ν_f are the Young’s modulus, and Poisson’s ratio of the FGM, respectively; E_c is the Young’s modulus of Ceramic.

The total potential energy can be obtained as follows:

$$\Pi = u + V, \tag{31}$$

where u is the potential energy of a normal deformable beam, and V is the potential energy of the external axially variable in-plane load. They can be determined as:

$$u = \frac{1}{2} \int_v \sigma_{xx} \varepsilon_{xx} dv = \frac{1}{2} \int_{-\frac{L}{2}}^{\frac{L}{2}} \left[A \left(\frac{du_0}{dx} \right)^2 - 2B \frac{du_0}{dx} \frac{d^2w_0}{dx^2} + C \left(\frac{d^2w_0}{dx^2} \right)^2 \right] dx, \quad (32)$$

$$V = -\frac{1}{2} \int_{-\frac{L}{2}}^{\frac{L}{2}} N_x^e(x) \left[\int_{-\frac{L}{2}}^x \left(\frac{dw_0}{dx} \right)^2 dx \right] dx. \quad (33)$$

Here, $N_x^e(x)$ - external axially variable in-plane load:

$$N_x^e(x) = N_0 \left[\alpha_1 \left(x + \frac{L}{2} \right)^2 + \alpha_2 \left(x + \frac{L}{2} \right) + \alpha_3 \right] = N_0 P(x). \quad (34)$$

Using Eqs. (31)–(34), the total potential energy can be obtained as follows:

$$\Pi = \frac{1}{2} \int_{-\frac{L}{2}}^{\frac{L}{2}} \left[A \left(\frac{du_0}{dx} \right)^2 - 2B \frac{du_0}{dx} \frac{d^2w_0}{dx^2} + C \left(\frac{d^2w_0}{dx^2} \right)^2 - N_0 P(x) \left\{ \int_{-\frac{L}{2}}^x \left(\frac{dw_0}{dx} \right)^2 dx \right\} \right] dx, \quad (35)$$

The stiffness coefficients are determined as below:

$$(A, B, C) = \int_{-\frac{h_s}{2}}^{\frac{h_s}{2}} (1, z, z^2) b_s Q_{11}^k dz. \quad (36)$$

In which A is the classical extensional, B is the bending and stretching coupling, C is the bending stiffness coefficients; b_s and h_s are the beam width and beam height, respectively.

Using the nodal degree of freedoms:

$$u_0 = N^u \Delta u_0, w_0 = N^w \Delta w_0, \theta_y = \frac{dw_0}{dx} = N^{\theta_y} \Delta \theta_y. \quad (37)$$

Substituting (37) into (35) leads to:

$$\Pi = \frac{1}{2} \{q_e\}_s^T ([K_e]_s + N_0 [K_{eG}]_s) \{q_e\}_s. \quad (38)$$

In which $[K_e]_s, [K_{eG}]_s$ are stiffness matrix and geometrical stiffness matrix of stiffener elements are given in Appendix A.

Using Lagrange's equations $\delta\Pi = 0$, from Eq. (38) we get the stability of stiffener elements:

$$([K_e]_s + N_0 [K_{eG}]_s) \{q_e\}_s = 0. \tag{39}$$

3.3. Stability analysis of SFG-CNTRC plate subjected to in-plane loading

Using the principle of direct stiffness matrix, combining the element matrices into the overall matrix, from Eqs. (26), (39) above, we have the stability equilibrium equation of SFG-CNTRC plate as follows:

$$([K] + \lambda [K_G]) \{q\} = 0, \tag{40}$$

where λ is the critical buckling load factor and called eigenvalue, and $[K], [K_G]$ are stiffness matrix and geometric stiffness matrix, respectively. They are defined as:

$$[K] = \sum_N ([K_e] + [K_{eG}]_s), [K_G] = \sum_N ([K_{eG}] + [K_{eG}]_s), \{q\} = \sum_N (\{q_e\} + \{q_e\}_s).$$

since, $\{q\} \neq 0$, then the determinant:

$$|[K] + \lambda [K_G]| = 0. \tag{41}$$

The minimum load that leads to the instability of the SFG-CNTRC plate is critical buckling load (p_{cr}), and is related to the lowest eigenvalue (λ_{cr}) as follows:

$$p_{cr} = \lambda_{cr} p_0. \tag{42}$$

The non-dimension critical buckling load is calculated through the critical buckling load and the geometric and material properties of the SFG-CNTRC plate as follows:

$$\bar{N} = \frac{p_{cr} a^2}{16 E^m h^3}, \tag{43}$$

where p_0 is the initial compressive loads value.

Hence, the bucking loads p_{cr} and the buckling modes were calculated using a MATLAB program named BUCKLING_2023.

The calculations in this paper have been undertaken to the FG-CNTRC plate to be under to identical and/or different support conditions on the four edges of the FG-CNTRC plate. The three boundary conditions used here are clamped - clamped - clamped - clamped (CCCC), simply - simply - simply - simply supported (SSSS), and clamped - free - free - free (CFFF) as examples below:

- (a) CCCC: at $x = 0, x = b: u = v = w = \theta_x = \theta_y = 0$, and at $y = 0, y = a: u = v = w = \theta_x = \theta_y = 0$;
- (b) SSSS: at $x = 0, x = b: w = \theta_x = 0$, and at $y = 0, y = a: w = \theta_y = 0$;

- (c) CFFF: at $x = 0$: $u = v = w = \theta_x = \theta_y = 0$, and at $x = b, y = 0, y = a$: All of DOFs are free.

4. RESULTS AND DISCUSSION

4.1. Comparison study

In this section, to evaluate the validity of the present FEM model in terms of critical buckling load, a comparison with numerical results available in the literature was performed. Accordingly, the obtained results were set in contrast with the results published by Georgantzinos et al. [27], based on various theories and methods. The studies an eight-layer symmetric cross-ply laminated rectangular plate with size ($a \times b \times h$) $100 \text{ mm} \times 100 \text{ mm} \times 1.016 \text{ mm}$, subjected to monoaxial vertical compressions and arranged in a ($\theta^\circ / -\theta^\circ$) lamination pattern, including different fiber orientation angles. The fundamental buckling mode of a laminated composite plate, which consisted of eight plies having a ($90^\circ / -90^\circ$) pattern. The plate is free (F) along the edges parallel to the y -axis, while the other edges are clamped (C). The epoxy resin 3501-6, multiwalled carbon nanotubes, and carbon fiber AS4 are chosen as matrix material, nanofillers, and fiber-reinforcing material, respectively. The material properties of the components constituting the nanocomposite material are shown in Table 1.

Table 1. Materials properties of the components [27]

Carbon Fiber AS4		Epoxy Resin 3501-6	
E_{11}^{CNT} (GPa)	225	E^m (GPa)	4.20
E_{22}^{CNT} (GPa)	15	G^m (GPa)	1.567
G_{12}^{CNT} (GPa)	15	ν^m	0.34
G_{23}^{CNT} (GPa)	7	ρ^m (g/cm ³)	1.25
ν_{12}^{CNT}	0.20		
ν_{23}^{CNT}	0.40		
ρ_{CNT} (g/cm ³)	1.80		

The mechanical properties of MWCNT-reinforced nanocomposite matrix are shown in Table 2.

Fig. 2 illustrates an exponential growth of the critical buckling load with an increase in fiber orientation angle from 0 to 90 degrees.

By comparison of the results above, as can be seen, a very good agreement is obtained.

Table 2. Mechanical properties of MWCNT-reinforced nanocomposite matrix [27]

V_{cnt} (%)	E_{11} (GPa)	E_{22} (GPa)	G_{12} (GPa)	G_{23} (GPa)	ν_{12}	ν_{23}	ρ (g/cm ³)
0.00	136.680	9.026	4.537	3.492	0.26	0.37	1.580
0.25	136.751	9.194	4.676	3.577	0.26	0.37	1.581
0.50	136.818	9.345	4.803	3.654	0.26	0.37	1.582
1.00	136.938	9.606	5.025	3.786	0.26	0.37	1.584
1.50	137.042	9.823	5.213	3.896	0.26	0.37	1.586
2.00	137.133	10.003	5.372	3.989	0.26	0.37	1.588
3.00	137.279	10.281	5.619	4.131	0.26	0.37	1.592
4.00	137.385	10.473	5.792	4.229	0.26	0.37	1.596
6.00	137.505	10.682	5.982	4.336	0.26	0.37	1.604
8.00	137.535	10.734	6.029	4.363	0.26	0.37	1.612
10.00	137.506	10.685	5.985	4.338	0.26	0.37	1.620

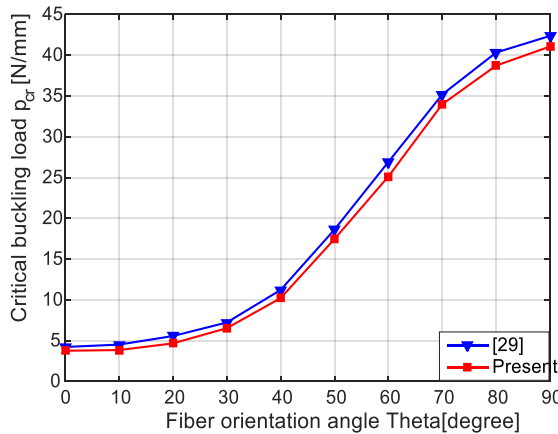


Fig. 2. Critical buckling load (p_{cr}) - fiber orientation angle relation (θ)

4.2. Numerical results

In this section, after validating the presented FEM model and methods above, a new study was carried out to analyze the static buckling of SFG-CNTRC plate subjected to uniform in-plane compression loads. As an example of buckling analysis, we used the SFG-CNTRC plate and boundary conditions presented in Section 4.1 with 12 stiffeners illustrated in Fig. 1. The stiffeners made of FGM with $E_m = 70$ GPa, $\nu_m = 0.3$ (Al), $E_c = 380$ GPa, $\nu_c = 0.3$ (Al₂O₃), and $h_1 = h_2 = h_s = 6$ mm, $S_1 = S_2 = 20$ mm, $d_1 = d_2 = b_s = 2$ mm.

Using the FEM model with 100 four-node plate elements for the plate and 50 two-node beam elements for stiffeners, a numerical calculation for the distribution uniform CNT pattern (UD) using two different plate theories consisting of four-variable refined

plate theory (present) and Mindlin plate theory was performed. The non-dimensional buckling load of SFG-CNTRC plate subjected to uniaxial compression ($\eta = 0, \zeta = 0$) and biaxial compression ($\eta = -1, \zeta = 0$) in $V_{cnt} = 2.0\%$ and CFFF boundary condition are listed in Table 3.

Table 3. The non-dimensional buckling load for two different plate theories under uniaxial compression ($\eta = 0, \zeta = 0$) and biaxial compression ($\eta = -1, \zeta = 0$) in $V_{cnt} = 2.0\%$ and CFFF boundary condition

(η, ζ)	Theory	Nondimensional buckling load	Different [%]
(0, 0)	Four-variable refined plate	8,003	3.07
	Mindlin plate	8,249	
(-1, 0)	Four-variable refined plate	7,173	3.09
	Mindlin plate	7,401	

The results in Table 3 demonstrate the critical buckling SFG-CNTRC plate load calculated by the four-variable refined plate theory is greater than that calculated by the Mindlin plate theory, it is this shows that using the results of the critical buckling loads of the SFG-CNTRC plate calculated by four-variable refined plate theory to recommend the operating load is safer than using the corresponding results calculated by Mindlin plate theory. On the other hand, the critical buckling SFG-CNTRC plate load under uniaxial compression ($\eta = 0, \zeta = 0$) is greater than that under biaxial compression ($\eta = -1, \zeta = 0$).

In this section, a numerical study was carried out to assess the influence of the CNT distribution along the layer thickness on the critical buckling load, according to which four typical FG-CNTRC plates (UD, FG-V, FG-O, and FG-X) were used to calculate. In Table 4, the non-dimensional buckling of SFG-CNTRC plate subjected to uniaxial compression ($\eta = 0, \zeta = 0$) for four typical CNT distributions along the layer thickness in different CNT volume fraction and boundary conditions are presented.

In all cases, the nondimensional buckling load is the largest in the case of the SFG-CNTRC plate with CCCC boundation condition and FG-X typical, in the case of CFFF boundation condition and FG-O typical the nondimensional buckling load of the SFG-CNTRC plate is the smallest. Furthermore, it is observed from the results that the non-dimensional buckling load of SFG-CNTRC plates increases with the increase of CNT volume fraction.

In this example, the effect of stiffener height ratio (h_s/h) on the non-dimensional buckling load of SFG-CNTRC plate has been studied. The ratio of h_s/h is varied from 0 to 10.0. The SFG-CNTRC plate subjected to uniaxial compression ($\eta = 0, \zeta = 0$) and in CFFF boundary condition, $V_{cnt} = 2.0\%$ and different typical FG-CNTRC plates. Results for

Table 4. The non-dimensional buckling load of SFG-CNTRC plate for four typical CNT distribution along the layer thickness in different CNT volume fraction and different boundary conditions

CNT pattern	V_{cnt} (%)	Nondimensional buckling load		
		CCCC	SSSS	CFFF
FG-O	0.5	7,418	6,253	5,140
	2.0	8,546	7,187	5,984
	4.0	10,170	8,736	7,097
FG-V	0.5	8,084	6,649	5,842
	2.0	9,466	7,535	6,723
	4.0	11,397	9,642	7,966
UD	0.5	9,898	8,482	6,986
	2.0	11,364	9,841	8,003
	4.0	13,477	11,738	9,492
FG-X	0.5	12,373	10,690	8,462
	2.0	14,124	12,076	9,683
	4.0	17,104	15,239	11,416

varied of the non-dimensional buckling load of SFG-CNTRC plates have been presented in Fig. 3.

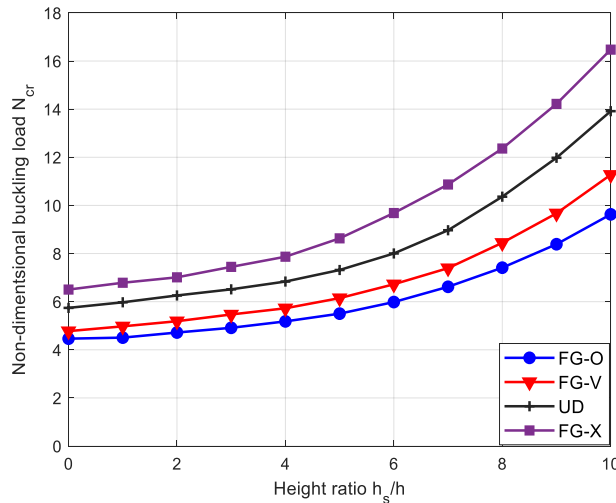
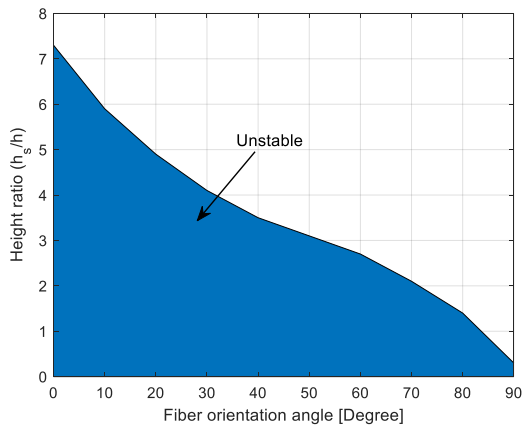


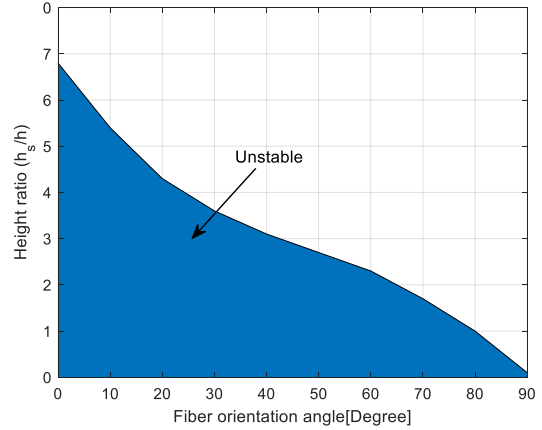
Fig. 3. Nondimensional buckling load as a function of ratio of stiffener height (h_s/h)

The fiber orientation angle (θ) and height ratio (h_s/h) influence the buckling property of the SFG-CNTRC plates. Their effects on unstable regions were also examined in this section. The variations in unstable regions of the SFG-CNTRC plate subjected to uniaxial

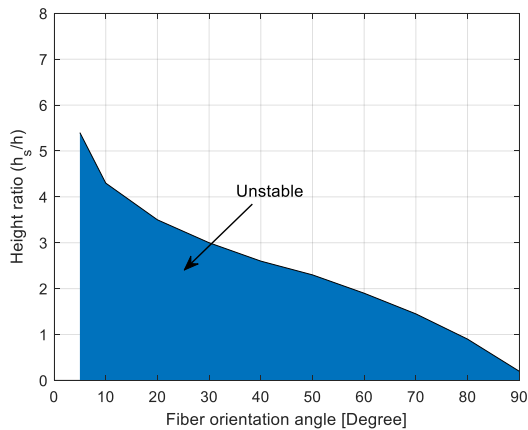
compression ($p_0 = 50 \text{ N/mm}$, $\eta = 0$, $\xi = 0$) in CFFF boundary condition and $V_{cnt} = 2.0\%$ with the fiber orientation angle (θ) and height ratio (h_s/h) are shown in Fig. 4.



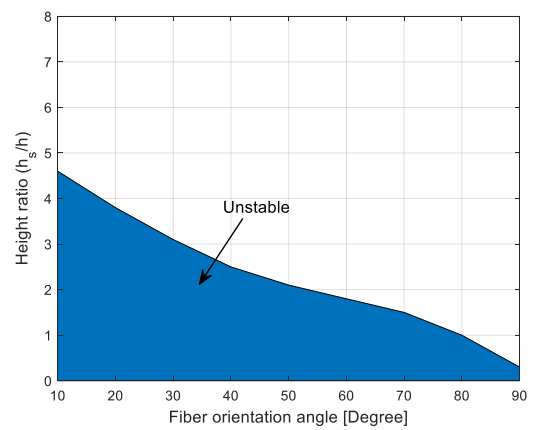
(a) SFG-CNTRC plate with FG-O typical



(b) SFG-CNTRC plate with FG-V typical



(c) SFG-CNTRC plate with UD typical



(d) SFG-CNTRC plate with FG-X typical

Fig. 4. Unstable regions for SFG-CNTRC plates subjected to uniaxial compression ($p_0 = 50 \text{ N/mm}$, $\eta = 0$, $\xi = 0$) in CFFF boundary condition and $V_{cnt} = 2.0\%$

5. CONCLUSIONS

In this study, the critical buckling load of SFG-CNTRC plates under in-plane static compression loads was investigated using FEM and a new four-variable refined plate theory. The results obtained from this research were in good agreement with the published results, this indicates that the algorithm and calculation program presented in this article are very reliable. The plate theory, CNT nanoparticles considerably, stiffer height ratio,

and fiber orientation angle influenced the critical buckling loads and unstable regions of the SFG-CNTRC plate. According to the numerical outcome, some general inferences are mentioned as follows:

- The stiffener system strongly enhances the critical buckling loads carrying capacity of the SFG-FGM plates. This to reach 115.7%, 136.1%, 142.4%, 153.3% with eight-layer symmetric crossply laminated rectangular FG-CNTRC plate with size 100 mm \times 100 mm \times 1.016 mm arranged in a $(\theta^0 / -\theta^0)$ lamination pattern, fiber orientation angle equal to 90 degrees, four typical FG-CNTRC (FG-O, FG-V, UD, and FG-X), respectively with and without stiffeners, subjected to monoaxial vertical compressions.

- The type of CNT has a strong effect on the buckling response of the SFG-CNTRC plates. According to, the critical buckling loads of the FG-X and UD CNTRC plates are larger than FG-V, FG-O CNTRC plates while the critical buckling loads of FG-X CNTRC are smallest through these four types of plates with the same mass fraction of CNT. In addition, the results show that the area of unstable regions of the FG CNTRC plate is the largest while this is the smallest for the FG CNTRC plate.

- In all cases, the fiber orientation angle of the composite layers has a great influence on the critical buckling loads of the FG-CNTRC plate, in the case of the FG-CNTRC plate subjected to uniaxial compression ($\eta = 0$, $\zeta = 0$) in CFFF boundary condition as above, it shows that the critical buckling loads are the largest when the fiber orientation angle equal to 90 degrees, while those the FG-CNTRC plate is easy to most unstable with the case the fiber orientation angle equal to 0 degrees.

DECLARATION OF COMPETING INTEREST

The authors declare that they have no known competing financial interests or personal relationships that could have appeared to influence the work reported in this paper.

FUNDING

This research received no specific grant from any funding agency in the public, commercial, or not-for-profit sectors.

REFERENCES

- [1] Z. X. Lei, K. M. Liew, and J. L. Yu. Buckling analysis of functionally graded carbon nanotube-reinforced composite plates using the element-free kp-Ritz method. *Composite Structures*, **98**, (2013), pp. 160–168. <https://doi.org/10.1016/j.compstruct.2012.11.006>.
- [2] N. T. Chung, H. X. Luong, and N. T. T. Xuan. Dynamic stability analysis of laminated composite plates with piezoelectric layers. *Vietnam Journal of Mechanics*, **36**, (2014), pp. 95–107. <https://doi.org/10.15625/0866-7136/36/2/3467>.

- [3] L. W. Zhang, Z. X. Lei, and K. M. Liew. Buckling analysis of FG-CNT reinforced composite thick skew plates using an element-free approach. *Composites Part B: Engineering*, **75**, (2015), pp. 36–46. <https://doi.org/10.1016/j.compositesb.2015.01.033>.
- [4] A. R. Shahidi, A. Anjomshoa, S. H. Shahidi, and E. E. Raeisi. Nonlocal effect on buckling of triangular nano-composite plates. *International Journal of Engineering*, **29**, (3), (2016), pp. 411–425.
- [5] R. Moradi-dastjerdi and H. Malek-Mohammadi. Free vibration and buckling analyses of functionally graded nanocomposite plates reinforced by carbon nanotube. *Mechanics of Advanced Composite Structures*, **4**, (1), (2017), pp. 59–73.
- [6] Ömer Civalek and M. Avcar. Free vibration and buckling analyses of CNT reinforced laminated non-rectangular plates by discrete singular convolution method. *Engineering with Computers*, **38**, (2020), pp. 489–521. <https://doi.org/10.1007/s00366-020-01168-8>.
- [7] A. M. Bash, S. E. Mnawe, and S. A. Salah. Numerical buckling analysis of carbon fibre-epoxy composite plates with different cutouts number by finite element method. *AIMS Materials Science*, **7**, (1), (2020), pp. 46–59. <https://doi.org/10.3934/mat.2020.1.46>.
- [8] N. V. Thanh. Nonlinear static stability of stiffened nanocomposite plate s subjected various types of loads. *VNU Journal of Science: Mathematics - Physics*, **38**, (2022). <https://doi.org/10.25073/2588-1124/vnumap.4685>.
- [9] T. Q. Minh, V. M. Duc, D. T. Dong, and V. H. Nam. Nonlinear buckling analysis of higher-order shear deformable FG-CNTRC plates stiffened by oblique FG-CNTRC stiffeners. *Vietnam Journal of Mechanics*, **44**, (2022), pp. 431–444. <https://doi.org/10.15625/0866-7136/17933>.
- [10] Z. Liu, C. Wang, G. Duan, and J. Tan. Isogeometric analysis of functionally graded CNT-reinforced composite plates based on refined plate theory. *Journal of Mechanical Science and Technology*, **34**, (2020), pp. 3687–3700. <https://doi.org/10.1007/s12206-020-0821-0>.
- [11] N. E. Meiche, A. Tounsi, N. Ziane, I. Mechab, and E. A. Adda.Bedia. A new hyperbolic shear deformation theory for buckling and vibration of functionally graded sandwich plate. *International Journal of Mechanical Sciences*, **53**, (2011), pp. 237–247. <https://doi.org/10.1016/j.ijmecsci.2011.01.004>.
- [12] H.-T. Thai and T. P. Vo. A new sinusoidal shear deformation theory for bending, buckling, and vibration of functionally graded plates. *Applied Mathematical Modelling*, **37**, (2013), pp. 3269–3281. <https://doi.org/10.1016/j.apm.2012.08.008>.
- [13] H.-T. Thai and S.-E. Kim. A simple higher-order shear deformation theory for bending and free vibration analysis of functionally graded plates. *Composite Structures*, **96**, (2013), pp. 165–173. <https://doi.org/10.1016/j.compstruct.2012.08.025>.
- [14] T. H. Daouadji, A. Tounsi, and E. A. A. Bedia. A new higher order shear deformation model for static behavior of functionally graded plates. *Advances in Applied Mathematics and Mechanics*, **5**, (2013), pp. 351–364. <https://doi.org/10.4208/aamm.11-m11176>.
- [15] N. T. Chung, D. T. N. Thu, and L. X. Thuy. Dynamic analysis of stiffened functionally graded composite plates reinforced by carbon nanotubes subjected to blast loads using a new four-variable refined plate theory. *International Journal of Computational Materials Science and Engineering*, **12**, (2022). <https://doi.org/10.1142/s2047684123500045>.
- [16] B. A. M. M. Selim, Z. Liu, and K. M. Liew. Active control of functionally graded carbon nanotube-reinforced composite plates with piezoelectric layers subjected to impact loading. *Journal of Vibration and Control*, **26**, (2019), pp. 581–598. <https://doi.org/10.1177/1077546319889849>.

- [17] H. Mallek, H. Jrad, M. Wali, A. Kessentini, F. Gamaoun, and F. Dammak. Dynamic analysis of functionally graded carbon nanotube–reinforced shell structures with piezoelectric layers under dynamic loads. *Journal of Vibration and Control*, **26**, (2019), pp. 1157–1172. <https://doi.org/10.1177/1077546319892753>.
- [18] H.-S. Shen. *Functionally graded materials: nonlinear analysis of plates and shells*. CRC Press, (2016).
- [19] F. Ebrahimi and A. Dabbagh. *Mechanics of nanocomposites: homogenization and analysis*. CRC Press, (2020).
- [20] H. Q. Tran, V. T. Vu, M. T. Tran, and P. Nguyen-Tri. A new four-variable refined plate theory for static analysis of smart laminated functionally graded carbon nanotube reinforced composite plates. *Mechanics of Materials*, **142**, (2020). <https://doi.org/10.1016/j.mechmat.2019.103294>.
- [21] C. N. Thai, T. T. Ich, and T. L. Xuan. Static and dynamic analysis of piezoelectric laminated composite beams and plates. In *Perovskite and Piezoelectric Materials*. IntechOpen, (2021). <https://doi.org/10.5772/intechopen.89303>.
- [22] J. N. Reddy. *Mechanics of laminated composite plates and shells*. CRC Press, (2003). <https://doi.org/10.1201/b12409>.
- [23] O. C. Zienkiewicz. *The finite element method*. Mc Graw Hill, International Editions, (1998).
- [24] N. N. Thuy and N. T. Chung. Dynamic analysis of smart stiffened composite plates using higher order theory. In *Proceedings of the 10th National Conference on Mechanics, Vietnam*, (2017), pp. 1197–1204.
- [25] S. Stoykov and P. Ribeiro. Stability of nonlinear periodic vibrations of 3D beams. *Nonlinear Dynamics*, **66**, (2011), pp. 335–353. <https://doi.org/10.1007/s11071-011-0150-z>.
- [26] J. G. Teigen. *Nonlinear analysis of concrete structures based on a 3D shear-beam element formulation*. PhD thesis, University of Eslo, (1994).
- [27] S. K. Georgantzinos, P. A. Antoniou, G. I. Giannopoulos, A. Fatsis, and S. I. Markolefas. Design of laminated composite plates with carbon nanotube inclusions against buckling: waviness and agglomeration effects. *Nanomaterials*, **11**, (2021). <https://doi.org/10.3390/nano11092261>.

APPENDIX A

$$[B] = \begin{bmatrix} \frac{\partial n^T}{\partial x} & 0 & -z \frac{\partial^2 N^T}{\partial x^2} & -f(z) \frac{\partial^2 N^T}{\partial x^2} \\ 0 & \frac{\partial n^T}{\partial y} & -z \frac{\partial^2 N^T}{\partial y^2} & -f(z) \frac{\partial^2 N^T}{\partial y^2} \\ \frac{\partial n^T}{\partial y} & \frac{\partial n^T}{\partial x} & -2z \frac{\partial^2 N^T}{\partial x \partial y} & -2f(z) \frac{\partial^2 N^T}{\partial x \partial y} \\ 0 & 0 & 0 & h(z) \frac{\partial N^T}{\partial y} \\ 0 & 0 & 0 & h(z) \frac{\partial N^T}{\partial x} \end{bmatrix},$$

Load type	Load symbol	α_1	α_2	α_3
Constant load	N_x^1	0	0	1
Linear Load-zero from left side	N_x^2	0	2	1
Linear Load-zero from right side	N_x^3	0	-2	2
Parabolic Load-zero from left side	N_x^4	3	0	0
Parabolic Load-zero from right side	N_x^5	3	-6	3
Symmetric Parabolic Load	N_x^6	-6	6	0

$$[K_e]_s = \begin{bmatrix} k_{u,u} & k_{u,w} & 0 \\ k_{u,w} & 0 & 0 \\ 0 & 0 & k_{\theta_y,\theta_y} \end{bmatrix}, \quad [K_{eG}]_s = \begin{bmatrix} 0 & 0 & 0 \\ 0 & k_{u,w} & 0 \\ 0 & 0 & 0 \end{bmatrix},$$

$$k_{u,u} = A \int_{-\frac{l}{2}}^{\frac{l}{2}} \frac{dN^{uT}}{dx} \frac{dN^u}{dx} dx, \quad k_{u,w} = -2B \int_{-\frac{l}{2}}^{\frac{l}{2}} \frac{dN^{uT}}{dx} \frac{d^2N^w}{dx^2} dx,$$

$$k_{\theta_y,\theta_y} = C \int_{-\frac{l}{2}}^{\frac{l}{2}} \frac{dN^{\theta_y T}}{dx} \frac{dN^{\theta_y}}{dx} dx, \quad k_{u,w} = \int_{-\frac{l}{2}}^{\frac{l}{2}} \left\{ - \int_{-\frac{l}{2}}^x P(x) \frac{dN^{wT}}{dx} \frac{dN^w}{dx} dx \right\} dx,$$

$$\bar{Q}_{11}^k = Q_{11}^k \cos^4 \theta^k + 2 \left(Q_{12}^k + 2Q_{66}^k \right) \sin^2 \theta^k \cos^2 \theta^k + Q_{22}^k \sin^4 \theta^k,$$

$$\bar{Q}_{12}^k = \bar{Q}_{21}^k = \left(Q_{11}^k + Q_{22}^k - 4Q_{66}^k \right) \sin^2 \theta^k \cos^2 \theta^k + Q_{12}^k \left(\sin^4 \theta^k + \cos^4 \theta^k \right),$$

$$\bar{Q}_{22}^k = Q_{11}^k \sin^4 \theta^k + 2 \left(Q_{12}^k + 2Q_{66}^k \right) \cos^2 \theta^k \cos^2 \theta^k + Q_{22}^k \cos^4 \theta^k,$$

$$\bar{Q}_{16}^k = \bar{Q}_{61}^k = \left(Q_{11}^k - Q_{12}^k - 2Q_{66}^k \right) \sin \theta^k \cos^3 \theta^k + \left(Q_{12}^k - Q_{22}^k + 2Q_{66}^k \right) \sin^3 \theta^k \cos \theta^k,$$

$$\bar{Q}_{26}^k = \bar{Q}_{62}^k = \left(Q_{11}^k - Q_{12}^k - 2Q_{66}^k \right) \sin^3 \theta^k \cos \theta^k + \left(Q_{12}^k - Q_{22}^k + 2Q_{66}^k \right) \sin \theta^k \cos^3 \theta^k,$$

$$\bar{Q}_{66}^k = \left[Q_{11}^k + Q_{22}^k - 2 \left(Q_{12}^k + Q_{66}^k \right) \right] \sin^2 \theta^k \cos^2 \theta^k + Q_{66}^k \left(\sin^4 \theta^k + \cos^4 \theta^k \right),$$

$$\bar{Q}_{44}^k = Q_{44}^k \cos^2 \theta^k + Q_{55}^k \sin^2 \theta^k, \quad \bar{Q}_{55}^k = Q_{44}^k \sin^2 \theta^k + Q_{55}^k \cos^2 \theta^k,$$

$$\bar{Q}_{45}^k = \bar{Q}_{54}^k = \left(Q_{55}^k - Q_{44}^k \right) \sin \theta^k \cos \theta^k.$$